Inner Structure of Starless Core L694–2 Derived from Millimeter-Wave Interferometry[1]

Daniel W.A. Harvey, David J. Wilner, Philip C. Myers

dharvey, dwilner, pmyers@cfa.harvard.edu

Harvard-Smithsonian Center for Astrophysics, 60 Garden Street, Cambridge, MA 02138

and

Mario Tafalla

m.tafalla@oan.es

Observatorio Astronómico Nacional, Alfonso XII 3, E-28014 Madrid, Spain

ABSTRACT

We study the density structure of the candidate contracting starless core L694–2 using 1.3 mm dust continuum observations from the IRAM Plateau de Bure Interferometer and the Berkeley-Illinois-Maryland Array, which probe spatial scales from 10000 AU to 500 AU. The long baseline PdBI observations detect no emission from the core, and limit the maximum contamination from a compact component $F_c < 2.7$ mJy. The flux limit corresponds to a very small disk mass, $M_{disk} \lesssim 5 \times 10^{-4}$ M$_\odot$ (60 K/T_{disk}), and bolsters the "starless" interpretation of the L694–2 core. The shorter baseline BIMA data are compared to a series of density models using a physically motivated temperature distribution with a central minimum. This analysis provides clear evidence for a turn-over from the steep density profile observed in the outer regions in dust extinction to substantially more shallow behavior in the inner regions (< 7500 AU). The best fit Bonnor-Ebert, Plummer-like, broken power law, and end-on cylinder models produce very similar flattened profiles and cannot be distinguished. We quantify the sensitivity of the inferred structure to various uncertainties, including the temperature distribution, the accuracy of the central position, and the presence of a weak unresolved central component. The largest uncertainty comes from the temperature assumption; an isothermal model modifies the best fit parameters by $\sim 2\,\sigma$, with the inferred density profiles more shallow. Dust emission and extinction profiles are reproduced by an embedded isothermal cylinder with scale height $H = 13.5''$ inclined at a small angle to the line of sight. The turn-over

observed in the L694–2 density distribution suggests that pressure forces still support the core, and that it has not fully relaxed as in the inside-out collapse model, despite the extended inward motions inferred from molecular line observations (Lee, Myers, & Tafalla 2001). In the context of the cylindrical density model, these inward motions may represent the contraction of a prolate core along its major axis.

Subject headings: ISM: globules — ISM: individual(L694) — radio continuum: ISM — stars: formation

1. Introduction

The observed properties of dense cores (e.g. Benson & Myers 1989) form the basis of the standard model of isolated star formation. In this model, the "starless" dense core represents the earliest identifiable stage of the star formation process. The physical conditions in this early stage have a profound impact on the evolution of protostars towards the main sequence. The initial density structure, particularly in the innermost regions, affects the collapse dynamics and the time dependence of the mass accretion rate and therefore many of the observable properties of protostars, including luminosity.

A quantitative understanding of the collapse dynamics has been hindered by uncertain knowledge of appropriate initial conditions (André, Ward-Thompson & Barsony 2000). In the popular theory of "inside-out" collapse, a spherical starless core loses turbulent and magnetic support and relaxes to a balance between gravity and thermal pressure, an r^{-2} density distribution is established and the core collapses from the inside-out with a constant mass accretion rate (Shu 1977). However, if collapse begins before the density distribution fully relaxes, then a central region of relatively constant density remains and the mass accretion rate is an order of magnitude larger at early times (Foster & Chevalier 1993). This phenomenon has been identified with the youngest "Class 0" protostars, which exhibit especially powerful outflows (Henriksen, Andre & Bontemps 1997; Andre, Ward-Thompson & Barsony 2000). Better observations of starless cores are needed to determine the initial conditions.

The L694–2 dense core is one of several "strong" infall candidates among starless cores, based on observations of molecular line profiles with redshifted self-absorption in a systematic search of more than 200 targets (Lee, Myers & Tafalla 1999). Molecular line maps of these objects provide strong evidence of inward motions, with speed ~ 0.1 km s^{-1} over a radius of ~ 0.1 pc (Lee, Myers & Tafalla 2001). The physical basis for these motions is unclear. The speeds are subsonic and may be associated with condensation through ambipolar diffusion, or perhaps a magnetically diluted gravitational collapse (Ciolek & Basu 2000). Alternatively, pressure driven motions due to the dissipation of turbulence may be responsible (Myers & Lazarian 1998).

Observations of dust column density provide a means to infer the structure and dynamical state of a dense core. Harvey et al. (2003b) describe near-infrared extinction measurements toward L694–2 that show a very steep density profile in the region $r = 30''$ to $83''$ (0.036 to 0.1 pc, or 7500 to 20000 AU), where background stars were detectable for extinction measurements. The extinction data can be fit by a number of models that produce nearly degenerate column density profiles, including a simple power law with index $p = 2.6 \pm 0.2$, a supercritical Bonnor-Ebert sphere with dimensionless outer radius $\xi_{\max} = 25 \pm 3$, or a nearly end-on isothermal cylinder with scale height $H = 13.5'' \pm 1.5''$. The latter two models provide a physical description of the core that represents an unstable configuration of material that is consistent with the infalling motions inferred from molecular spectral line profiles. In particular, the slightly tilted cylindrical model that provides a basis for interpreting the asymmetry of the L694–2 core should be highly unstable to gravitational collapse along its axis (close to the line of sight), consistent with the strength and orientation of the observed velocity structure. The model also provides a framework for understanding the very high extinctions observed in L694–2, namely that the core has prolate structure with the full extent (mass) of the core being missed by analysis that assumes symmetry between the profile of the core in the plane of the sky, and the profile of the core along the line-of-sight.

Observations of long wavelength dust emission provide another means of probing density structure. This technique is almost as direct as observations of dust extinction. The intensity of the optically thin emission provides an integral along the line-of-sight of the product of the density, temperature, and opacity of the dust. The analysis of dust emission complements dust extinction work because the dust emission method becomes most effective in the high column density inner regions of dense cores where dust extinction becomes large and difficult to penetrate.

Much of the detailed information on starless core structure comes from observations of dust emission, using data from bolometer cameras (e.g. Ward-Thompson, Motte & Andre 1999, Shirley et al. 2000, Visser, Richer & Chandler 2001). An important conclusion from

these studies is that starless cores appear to show flat density profiles in their inner regions, with extended envelopes that fall off rapidly in power law fashion. Recently, the predominance of the flat central density gradients has been called into question as more sophisticated analysis including self-consistent temperature calculations indicate much smaller regions of flattening, or no flattening at all, in large part because the cores are cooler in their deep interiors than assumed previously (Evans et al. 2001, Zucconi et al. 2001). In addition, the central regions of even the nearest protostellar cores are generally comparable in size to the beamwidths of these telescopes and are poorly resolved. The density structure at smaller scales can be probed with interferometers. Strong constraints can be derived by analyzing interferometer data from dense cores directly in the visibility domain, though this approach has been rarely used (Keene & Masson 1990, Hogerheijde et al. 1999, Harvey et al. 2003a, Looney, Mundy & Welch 2003).

L694–2 has been mapped at 850 μm with SCUBA on the JCMT by Visser (2000) and at 1.2 mm with the IRAM 30m by Tafalla et al. (2003). The two maps have similar resolutions, 14" for SCUBA and 11" for IRAM. The dust emission profiles suggest a steep outer density gradient ($p \simeq 2.7$ from SCUBA, $p = 2.5$ from IRAM) consistent with that inferred from dust extinction (Harvey et al. 2003b). The usual isothermal analysis suggest a flattening of the density gradient within a radius of a few thousand AU. Visser (2000) fits a broken power law model that suggests an inner power law index of $p = 0.8$ within a break radius of 8000 AU ($\sim 30''$). Although no radio point source has been detected in the L694–2 core (e.g. Harvey et al. 2002), the measurement of the inner power law index suffers a potentially large systematic error from possible point-source contamination to the central beam (Shirley et al. 2002). In this paper, we present observations of dust continuum emission from L694–2 at 1.3 mm obtained with the IRAM Plateau de Bure Interferometer (PdBI) and the Berkeley-Illinois-Maryland-Array (BIMA). The long baseline observations from the PdBI limit the contribution to the flux from any embedded point source, while the BIMA observations sample the dense core structure on size scales from ~ 10000 AU to ~ 1500 AU (resolution to 6"). Together, these observations provide conclusive evidence of a flattening in the density profile within $\sim 30''$ from the center of the core.

2. Observations

2.1. IRAM PdBI

Continuum emission from L694–2 was observed at 1.3 mm (231.32 GHz) with the IRAM PdBI in the compact D configuration on 2001 November 20 (4 antennas) and 2002 April 03 (6 antennas). Table 1 lists the observational parameters. A single pointing was used, with

center 19:41:04.44, 10:57:00.9 (J2000) chosen to coincide with the position of peak emission in the $N_2H^+(1-0)$ spectral line measured at BIMA (Jonathan Williams, private communication). The half-power field of view for PdBI at this wavelength is $22''$ (5500 AU). The PdBI observations provide measurements at baseline lengths from the shadowing limit of 15 m to a maximum of over 100 m (resolution $\sim 2''.6$). The absolute flux scale was set by observations of the standard source MWC 349, assumed to be 1.71 Jy. The estimated uncertainty in the flux scale is roughly 20%. Frequent observations of nearby calibrators J1751+096 and J1925+211 were used to determine time-dependent complex gains. Continuum visibility records were formed for each 60 s integration of the digital correlator (3×160 MHz bandwidth, tuning double sideband). The correlator bandpass was measured with observations of the strong sources 3C 345 (2001 November 20) and 3C 273 (2002 April 03). The data were calibrated using the IRAM software package *CLIC*, and comprise a total of 7240 records (2040 records from 2001 November 20, 5200 from 2002 April 03). In addition to amplitude and phase, each record contains a variance measure, determined from the system temperature and antenna gains.

2.2. BIMA

Continuum emission from L694–2 was observed at 1.3 mm (231.32 GHz) with BIMA in the compact D configuration on 2001 September 22 and 29, 2002 June 08, and 2002 September 09, and in the more extended C configuration on 2002 March 31. Table 1 lists the observational parameters. A single pointing of the nine antennas was used on each occasion. The pointing center for the BIMA observations is displaced from the PdBI pointing, by δR.A.$= -1''.8$, δDec.$= 5''.2$. The half-power field of view for the BIMA antennas is $50''$ (12,500 AU). The BIMA observations provide measurements at baseline lengths from the shadowing limit of 6 m to a maximum of 70 m (resolution $\sim 3''.7$). The bandpass and flux calibration were determined through observations of Uranus, using the a priori antenna gains. The estimated uncertainty in the flux scale is roughly 15%. Frequent observations of J1925+211 were used to determine time-dependent complex gains. Continuum visibility records were formed for each 23 s integration of the digital correlator (700 MHz bandwidth). The data were calibrated in the BIMA software package *MIRIAD*. The resulting $\sim 2 \times 10^5$ records were then averaged in time bins of 3.45 minutes (9 records). This choice of binning was made to reduce the number of visibilities to a more manageable size for analysis, without introducing significant phase error at the longer baselines. The resulting dataset contains 22327 records. As with the PdBI dataset, a variance measure for each visibility measurement is also recorded.

3. Constructing Model Visibilities

The visibility measurements are analyzed directly, without producing images that are limited by standard Fourier inversion and deconvolution techniques. This approach is computationally intensive, but it allows a much more direct comparison with models than analyzing images. In particular, the results are not compromised by problems with the synthesized beam characteristics and dynamic range.

The L694–2 visibilities are compared to theoretical models of protostellar envelope structure by constructing synthetic visibilities, taking account of (1) the dust continuum radiative transfer, and (2) the specifics of the observations, including the exact (u, v) sampling and primary beam pointing and attenuation for the two telescopes. The models necessarily include an assumed temperature distribution and (constant) specific mass opacity in addition to the model density field. We do not consider an exhaustive list of starless core models but instead fix attention on a few widely promoted density fields, including Bonnor-Ebert spheres, Plummer-like models, broken power law descriptions, and isothermal cylinders. These models can all match the steep density gradient inferred for the outer regions of the core.

The model datasets are constructed using the recipe described in Harvey et al. (2003a). In brief, a 512×512 model intensity image of resolution $0\rlap{.}''5$ pixel^{-1} is calculated using the full Planck function for the emissivity and integrating the radiative transfer equation through the model globule. Each model is normalized to a flux at 1.2 mm of 800 ± 80 mJy within a circular aperture (top-hat) of radius $30''$, calculated from the continuum map of L694–2 made by Tafalla et al. (2003) with MAMBO on the IRAM 30m (assuming a dust opacity spectral index of unity). We adopt an outer boundary of $R_{\mathrm{out}} = 0.15$ pc in the models based on the extinction observations (Harvey et al. 2003b), although the results are not sensitive to this assumption. Observations are simulated by performing an FFT, and assuming a Gaussian form for the primary beams (PdBI FWHM $22''$, BIMA FWHM $50''$). The exact (u, v) sampling is achieved by interpolating the real and imaginary parts of the resulting visibility grid. The center for each model is assumed to be at the pointing center of the PdBI observations, and in Section 5.2.1 we discuss the slight sensitivity of the results to this assumption.

3.1. Model Selections

As detailed above, the model visibilities are derived from the assumed (1) mass density distribution $\rho(r)$, (2) dust temperature distribution $T_d(r)$, and (3) specific mass opacity of

the dust $\kappa_{1.3\ \mathrm{mm}}$ (normalized to a constant flux within a $30''$ circular aperture). We consider the expected form of these quantities, and their uncertainties.

3.1.1. Density

The main goal is to constrain the density distribution of L694–2, given a realistic choice for the temperature distribution, and specific mass opacity. We consider four models of starless core density structure that can match the steep density gradient in the outer regions inferred from the near-infrared extinction.

Bonnor-Ebert spheres.— These models are pressure-confined isothermal spheres, for which the solution remains finite at the origin (Ebert 1955, Bonnor 1956). They are solutions of a modified Lane-Emden equation (Chandrasekhar 1967):

$$\frac{1}{\xi^2}\frac{d}{d\xi}\left(\xi^2\frac{d\psi}{d\xi}\right) = \exp\left(-\psi\right), \tag{1}$$

where $\xi = (r/R_0)$ is the dimensionless-radius, $R_0 = a/\sqrt{4\pi G\rho_c}$ is the (physical) scale-radius, and $\psi(\xi) = -\ln\left(\rho/\rho_c\right)$ is a logarithmic density contrast, with ρ_c the (finite) central density, and a is the effective sound speed in the core (we adopt $a = 0.20$ km s^{-1} based on an assumed central temperature of 9 K, with turbulent component $a_{\mathrm{turb}} = 0.09$ km s^{-1}, as in the extinction study). Configurations with $\xi_{\mathrm{max}} > 6.5$ are unstable to gravitational collapse. A highly supercritical dimensionless-radius of $\xi_{\mathrm{max}} = 25 \pm 3$ was found to reproduce the extinction observations of L694–2 for radii $r \geq 30''$.

Plummer-like models.— These are empirical models suggested by Whitworth & Ward-Thompson (2001) that capture the essential observed properties of starless cores with a minimum of free parameters. The model assumes that when a prestellar core becomes unstable against collapse at time t=0, it is static and approximates to a Plummer-like density profile (Plummer 1911), of the form:

$$\rho(r,t=0) = \rho_0\left[\frac{R_0}{(R_0^2 + r^2)^{1/2}}\right]^\eta \tag{2}$$

The initial density is therefore uniform for $r \ll R_0$, and falls off as $r^{-\eta}$ for $r \gg R_0$. Whitworth & Ward-Thompson (2001) propose a fixed value of $\eta = 4$ in the model in order to reproduce the relative lifetimes and accretion rates for the Class 0 and Class I phases. For L694–2, the density power law index in the outer regions inferred from near infrared extinction is $p = 2.6\pm0.2$ if the core is assumed to be unobscured, but has a steeper value of $p = 3.7\pm0.3$ if the core is embedded in a more extended uniform distribution of material, as is suggested by

the flattening in the radial profile beyond $r \gtrsim 0.1$ pc (Harvey et al. 2003b). A Plummer-like core with $\eta = 4$ embedded in a more extended cloud can therefore reproduce the extinction observations. The scale radius R_0 is not constrained by the extinction measurements because no flattening is evident in the data (which do not penetrate the $r \lesssim 30''$ inner region).

Broken Power Law models.— These models represent a variation of the Plummer-like model, to allow for an inner density power law index that is non-zero. The density distribution we adopt is of the form:

$$\rho(r) = \frac{\rho_0}{((r/R_0)^{(2p)} + (r/R_0)^{(2\eta)})^{(1/2)}} \tag{3}$$

For $r \ll R_0$, the density falls off as r^{-p}, and for $r \gg R_0$, the density falls off as $r^{-\eta}$. We choose this continuous prescription to prevent discontinuities in the first derivatives (which show up in the visibility profile) that would result from including a unphysical sharp break in the density distribution. We choose $\eta = 2.6$ to reproduce the observed extinction without introducing additional structure components. There is some degeneracy between R_0 and p in the resulting visibility (or intensity) profile, since decreasing R_0 or increasing p both produce a steeper emission profile or a flatter visibility profile. The visibility amplitude for a typical starless core profile falls rapidly and is already very low at baselines that are long enough to sample the inner structure that cannot be probed with extinction. Even the high quality visibility dataset that we have obtained from BIMA and the PdBI therefore does not provide sufficient sensitivity to constrain both parameters simultaneously. We therefore choose a fixed value of $R_0 = 30''$ in order to quantify the effect of the inner power law index p. This choice is made on the basis that $R_0 = 30''$ is the largest value of R_0 that is consistent with the extinction data, which will lead to the largest possible value of p allowed by the dataset (since a smaller value of R_0 will necessarily require a shallower p to produce a given visibility amplitude at a given baseline).

Cylinder models.— The isothermal cylinder model is a two dimensional analog of the Bonnor-Ebert sphere. The density is a function of the radial coordinate only (Ostriker 1964):

$$\rho(r, z) = \frac{\rho_c}{(1 + (r^2/8H^2))^2} \tag{4}$$

where $H = a/\sqrt{4\pi G \rho_c}$ is the scale height that is equivalent to the scale radius R_0 in the B-E analysis. The density is uniform near the axis of the cylinder but decays ever more rapidly with increasing radius, asymptoting to a power law of index $p = 4$ for $r \gg H$. The filament is supported radially by pressure gradients, but is unstable in the direction along its axis. The density distribution of the isothermal cylinder is a two dimensional case of the Plummer-like model, with $\sqrt{8}H = R_0$, and with a physical basis for the normalization of the density

profile. A cylindrical model can therefore reproduce the observational properties of prestellar cores that provided the motivation for the Plummer-like models. In addition, because the isothermal cylinder and the B-E sphere both represent equilibria between self-gravity and gas pressure, the spherically averaged density profile of an isothermal cylinder can also mimic closely that of a B-E sphere, in particular a flat inner region with a steeply falling envelope (Boss & Hartmann 2001). The cylindrical model also provides a basis for interpreting the departures from spherical symmetry in the L694–2 core (Harvey et al. 2003b). A slightly tilted, embedded cylinder with scale height $H = 13.5'' \pm 1.5''$ reproduces the extinction profile for the inner $83''$ (0.1 pc) of the core. In the present study we consider isothermal cylinders viewed along the axis, since the subtle effect of a small tilt angle can not be constrained with the visibility dataset.

3.1.2. Extended Cloud Structure

Both Plummer-like and Isothermal Cylinder models can successfully describe the near-IR extinction observations, if the cores are embedded in an extended distribution of gas. This additional component to the density structure is suggested by the shape of the radial extinction profile, and must be accounted for in the fitting of these types of model. We include the extended cloud structure in the visibility analysis as follows. The extended structure is assumed to be smooth and is therefore resolved out by the interferometers. The only effect of the additional structure is to reduce the total flux that is attributable to the core in this context. The extinction profile of the L694–2 core asymptotes to a color-excess that is approximately 0.2 magnitudes higher than the background, and about a tenth (1/10) of the color excess at $30''$ radius (the edge of the flux normalization aperture). We approximate the intensity profile to be flat within $30''$ of the core, and assume that the temperature of the extended gas is equal to that in the core, so that the extended structure accounts for 10% of the flux normalization for each of these types of model.

3.1.3. Temperature

A detailed study of the expected dust temperature distribution in starless cores has been performed by Evans et al. (2001). They calculate the temperature distribution, $T_d(r)$, self-consistently using a 1D radiative transport code, and assuming Ossenkopf & Henning (1994) opacities for grains that have grown by coagulation and accretion of thin ice mantles. They find that the Interstellar Radiation Field (ISRF) dominates the heating in the core, roughly a factor of 3 stronger than heating due to cosmic rays, even at the center of an

opaque core. The effect of the opacity law on $T_d(r)$ is small; the largest difference is at the center of the core, where opacities for coagulated grains that lack mantles cause a lower value of T_d by ~ 0.5 K.

Evans et al. (2001) present the dust temperature distribution $T_d(r)$ for a Bonnor-Ebert sphere with outer radius $R_{\rm out} = 0.17$ pc (35000 AU) in which the gas is isothermal at 10 K (their Figure 3). The model has a central density of $n = 1 \times 10^6$ cm^{-3}, and a dimensionless outer radius of $\xi_{\rm max} \simeq 42$, and is heated by an ISRF that combines the infrared behavior from COBE (Black 1994) and the ultraviolet behavior from Draine (1978). The dust temperature varies from a minimum of ~ 8 K in the inner thousand AU of the core, to a maximum of ~ 14 K in the outer regions. The model is similar in radius, but somewhat more centrally condensed than the B-E sphere that best fits the extinction in L694–2 ($R_{\rm out} = 0.17$ pc, $R_0 = 3.4''$ in the computed model; $R_{\rm out} = 0.15 \pm 0.14$ pc, $R_0 = 4.9'' \pm 0.6''$ for L694–2). In addition, the Evans et al. (2001) analysis neglects any shielding by an extended component of material that surrounds the core, as is seen around L694–2 in near-infrared extinction (Harvey et al. 2003b). The degree to which the interior of the L694–2 globule is shielded from the ISRF will differ somewhat from in the Evans et al. (2001) model. However, the Evans et al. (2001) model likely provides an accurate description of the actual temperature profile in L694–2 to within the uncertainties that stem from the inhomogeneities of the ISRF. We therefore adopt the Evans et al. (2001) temperature distribution for use in our modeling. We investigate the sensitivity to the assumed temperature distribution by also exploring models that assume a constant dust temperature of $T_d = 12$ K.

The Bonnor-Ebert and Cylinder models used in the model fitting are based on hydrostatic equilibrium density configurations for a gas cloud that has an isothermal kinetic temperature T_K. The Evans et al. (2001) temperature distribution is calculated using a density model that obeys the same assumption. At high densities efficient gas-dust coupling forces T_K to equal the dust temperature T_d, while at low densities ($n \lesssim 10^4$ cm^{-3}) $T_K \neq T_d$ (Takahashi, Silk, & Hollenbach 1983, Doty & Neufeld 1997). The Bonnor-Ebert model that best fits the L694–2 extinction has central density $n \sim 3 \times 10^5$ cm^{-3}, with a center-to-edge density contrast of ~ 400. In the inner regions of L694–2 the kinetic temperature of the gas should decrease in a similar fashion to the dust temperature, but in the outer regions the two temperature distributions may depart. An entirely self-consistent approach to the problem would include a full calculation of the gas energetics, including dust coupling to calculate simultaneous density and (dust) temperature distributions. Such an approach has been followed by Galli, Walmsley & Gonçalves (2002). However, to zeroth order, small departures from isothermality in the kinetic temperature have little effect on the density profile, since the pressure gradient of the gas is dominated by the gradient in the density and not the temperature. The effect of non-isothermality on the resulting emission profile is

therefore dominated by the dust temperature dependence of the Planck function. Since the uncertainties that surround the calculation of the dust temperature profile are substantial, the computational overhead of a more self-consistent approach is not justified at this time. We separate the problem into two parts, modeling density profiles assuming a constant gas kinetic temperature, but relaxing the isothermal assumption in order to model the resulting thermal emission from the core.

A remaining issue deals with the appropriate temperature distribution to use for the cylindrical models, since these are by definition not spherically symmetric. Since no self-consistent 3D dust radiative transfer results are available for this type of model, we have made a very simple approximation, assuming the filament to have an aspect ratio of 2:1 and stretching the Evans et al. (2001) temperature distribution appropriately along the line-of-sight.

3.1.4. Mass Opacity

The mass opacity of dust grains in the millimeter region of the spectrum in protostellar envelopes is uncertain but generally assumed to follow a power law with frequency, $\kappa_\nu \propto \nu^\beta$. The power-law index varies depending on the dust properties, but tends to be bounded by a small range, roughly 1 to 2 (Ossenkopf & Henning 1994). The opacity of the dust affects the temperature distribution of the dust, as already described. For our purposes, only the spectral index is of importance, since we assume a constant opacity (independent of r), and the overall normalization is fixed by matching the MAMBO single dish observation. The spectral index affects the normalization of the models only weakly since the MAMBO flux constraint is made at a wavelength very close to that of the PdBI and BIMA observations. We have adopted $\beta = 1$; the extreme alternative of $\beta = 2$ leads to only a 4% change in flux normalization (for $T_d = 12$ K), which is small compared to the overall 10% uncertainty in the normalization itself.

4. Method for Fitting Model Parameters and Evaluating Fit Quality

The basic procedure is to maximize the probability distribution:

$$P(\text{Model} \,|\, \text{data}) = \prod_i e^{-(Z_i - f(x_i; p, m))^2 / 2\sigma_i^2} \, e^{-(m - m_0)^2 / 2\sigma_m^2} \tag{5}$$

where the Z_i are the visibility data points with uncertainty σ_i, $f(x_i; p, m)$ are the model data points, p a free parameter in the models, and m a model parameter about which

we have a constraint (namely that it is a Gaussian random variable with mean m_0 and standard deviation σ_m). Maximizing the probability distribution is equivalent to minimizing the logarithm of its inverse. Taking account the fact that the Z_i are by nature complex visibilities, we want to minimize a modified χ^2:

$$\tilde{\chi}^2 = \sum_i \frac{|Z_i - f(u, v; p, m)|^2}{\sigma_i^2} + \frac{(m - m_0)^2}{\sigma_m^2} \qquad (6)$$

The sum/product can extend over any suitable subset of the visibility points. It is useful to be more explicit about the parameters p & m. The free parameter p is used to describe the shape of the model, e.g. the index of the inner part of the broken power-law density distribution. The parameter m allows us to include the observational uncertainties, e.g. the $\sim 10\%$ uncertainty in the normalization of the models derived from the Tafalla et al. (2003) map, and the $\sim 15\%$ uncertainty in the flux calibration for the BIMA data. This is achieved by allowing the BIMA model visibilities to be scaled by a constrained parameter m, assumed to be a Gaussian random variable with mean $m_0 = 1.0$ and standard deviation $\sigma_m = 20\%$. The longer baselines of PdBI do not detect any signal from the L694–2 core. These measurements are used to constrain a limit on the point source contamination and are not included in the model fitting.

For a given model, we evaluate the best fit parameters by minimizing the modified χ^2 distribution. Uncertainties in the parameter values are analyzed using the Monte Carlo technique known as the *bootstrap* (Press et al. 1992). In brief, the dataset is resampled n times (typically $n \sim 200$), each time the fitting process is repeated and the best-fit parameters recorded, until the distribution of best-fit parameters is well sampled. The width of the distribution provides an estimate of the uncertainty in the parameters that best fit the original dataset.

This numerical approach is made necessary by the non-linear nature of the fitting parameters, and is especially useful for this analysis because small variations in the value of the modified χ^2 as defined above may represent surprisingly large variations in fit quality. The nature of the visibility dataset, comprising a very large number of very low signal-to-noise measurements, means that even a model with zero signal will on average reproduce each visibility measurement to within its uncertainty. The resulting shallowness of the χ^2 wells causes two models with slightly differing parameters to seem almost equally good despite the fact that there is ample signal to distinguish them. The numerical approach essentially bypasses this complication. The issue could also be circumvented by binning the visibilities (e.g. radially in (u, v) distance), to increase the signal-to-noise, and then performing a χ^2 fit to the binned values. We avoid this solution because the visibility profiles for the various models are falling steeply at the baselines of interest, and binning the data inevitably intro-

duces a bias in the fit due to contracting the range of baseline vectors to a single length at the center of the bin. We use binning only as a graphical tool in order to demonstrate the fit quality of a particular model.

5. Results and Analysis

5.1. Limits on Point Source Flux

The PdBI dataset covers baselines from 12 to 80 kλ, with an overall rms noise of 0.9 mJy. The visibility data are consistent with the noise. The long baselines covered by the PdBI data therefore provide an important constraint on the maximum compact component of the flux from the L694–2 core, $F_c < 2.7$ mJy (3 σ). For optically thin dust, this limiting flux corresponds to an implied (disk) mass limit of $M \lesssim 5 \times 10^{-4}$ M$_\odot$ (60 K/T_{disk}) for an opacity $\kappa_{1.3\ \mathrm{mm}} = 0.02$ cm^2 g^{-1}. This limit is roughly an order of magnitude lower than the 0.002–0.3 M$_\odot$ range of disk masses observed around T-Tauri stars by Beckwith et al. (1990), and further demonstrates the "starless" nature of the L694–2 core.

The flux limit allows an estimate of the maximum bolometric luminosity for any compact component embedded in the L694–2 core. For a simple estimate, we assume a dust opacity spectral index of unity, and model the compact component as a graybody of the form:

$$F_\nu = B_\nu(\langle T_{\mathrm{dust}} \rangle) \left(1 - \exp[-\tau_\nu]\right) \Omega_S \ , \tag{7}$$

where $B_\nu(\langle T_{\mathrm{dust}} \rangle)$ denotes the Planck function at frequency ν for a mean dust temperature $\langle T_{\mathrm{dust}} \rangle$, τ_ν is the dust optical depth, and Ω_S the solid angle subtended by the source (e.g. Beckwith et al. 1990). Since the envelope is entirely optically thin at 1.3 mm, the graybody must have a flux that is ≤ 2.7 mJy at this wavelength. For a given mean dust temperature, this constraint fixes the mass of the compact component. The only remaining parameter is the radius R of the component, which essentially identifies the wavelength at which the emission becomes optically thick.

For a compact component to remain undetected in our PdBI observations implies that its bolometric luminosity is:

$$L_{\mathrm{bol}} \lesssim 0.07 \ \mathrm{L}_\odot \ (R/100 \ \mathrm{AU})^{0.1} \ (\langle T_{\mathrm{disk}} \rangle / 50 \ \mathrm{K})^{3.9} \tag{8}$$

Note that these power law dependencies are an approximation and are not accurate for changes in the parameters by factors of more than ~ 2. The dependences on temperature and radius can be understood in the following way. The dominant contribution to the luminosity comes from the R-J region of the Planck function, in which the emission is optically thin

(for this typical size scale and temperature, the compact component becomes optically thick slightly to the Wien side of the peak in the Planck function). If the emission from beyond the peak in the Planck function is entirely negligible, then the luminsosity is proportional to: $L \propto \int_0^{\nu_{\max}} \kappa_\nu \nu^2 d\nu$. Note that the flux constraint at 1.3 mm causes there to be no temperature dependence in the integrand. Using the Wien law for $\nu_{\max} \propto \langle T \rangle$, and $\kappa_\nu \propto \nu$, then gives $L_{\mathrm{bol}} \propto \langle T \rangle^4$. The contribution of the optically thick emission causes the actual temperature dependence to depart from this relation, and introduces a weak dependence on the radius of the compact source.

The limit the PdBI observations place on the maximum bolometric luminosity of any embedded compact object is substantially lower than the IRAS limit for L694–2 of ~ 0.3 $L_\odot$. Reprocessing of the warm compact emission to long wavelengths by the envelope essentially allows a large bolometric luminosity to remain hidden below the IRAS detection limit.

5.2. Density Structure

The PdBI data constrains the maximum compact component of dust emission, which allows us to proceed to fit for the envelope structure using the BIMA data at shorter baselines. The envelope visibility profiles fall steeply with increasing baseline. (Note that a flatter emission profile leads to a steeper visibility falloff.) At the longer BIMA baselines, the visibility amplitudes for the best fit models falls well below the signal-to-noise of the entire BIMA dataset. This makes restricting the visibility fitting to the shorter baselines advisable, since extending the fitting range to longer baseline adds noise but no signal. Having experimented with various upper limits on the baseline length, we found that an upper limit of 10 kλ was optimal. Increasing the upper limit to 15 kλ, or 20 kλ did not change the results but produced higher values of the reduced χ^2. The visibility dataset to which the models were fit contains 6424 visibility measurements (each a 3.45 minute integration) and covers baselines from 5 to 10 kλ. The rms noise in this reduced dataset is 3.3 mJy. Table 2 summarizes the results from the χ^2 fits to the four types of model described in Section 3.1. Below we describe these results.

Bonnor-Ebert Sphere.— the model that best fits the visibility data has dimensionless outer radius $\xi_{\max} = 18\,^{+3}_{-4}$ (Fit I). At the 2 σ level this is consistent with the results of the extinction study, where a B-E sphere with $\xi_{\max} = 25 \pm 3$ reproduced the observed color excess.

Plummer-like model.— the embedded model that best fits the visibility data has scale radius $R_0 = 26''\,^{+4}_{-3}\,''$, or 6500^{+1000}_{-750} AU (Fit II). This turn-over radius is consistent with the

Visser (2000) analysis of SCUBA data, which fit a broken power law with a transition to a shallower index within a break radius of $\sim 32''$ (8000 AU).

Broken Power law.— the model that best fits the visibility data has a power law index in the inner region ($r < 30''$) of $p = 0.9\,^{+0.12}_{-0.16}$ (Fit III). The turn-over radius used in this model is similar to that from the Visser (2000) analysis, and the fitted inner power law index is consistent with their result of $p = 0.8$ (no uncertainties are given), despite their use of an isothermal dust temperature distribution. Note that the use of a smaller turn-over distance results in a lower fitted value of p. The above result should therefore be construed as a "mean" index in the $r < 30''$ (7500 AU) region, or as an upper limit on the power law index in the innermost regions.

Cylinder.— the end-on cylindrical model that best fits the visibility data has scale height $H = 12''\,^{+3.0}_{-1.5}\,''$, or 3000^{+750}_{-400} AU (Fit IV). This is consistent with the results of the extinction study, where a slightly tilted cylinder with $H = 13.5'' \pm 1.5''$ best matched the observed color excess.

For each of the best fit models, the fitted value of the scaling parameter is $m \simeq 0.9 \pm 0.05$. That the preferred value is similar for each model and not unity suggests that the data prefer a particular slope of visibility profile that when extrapolated back to zero baseline has 10% lower normalization than the MAMBO flux. This difference is well within the combined uncertainties of the MAMBO flux measurement and the BIMA calibration accuracy (total $\sim 20\%$).

Figure 1 shows plots of visibility amplitude vs. (u, v) distance for the various best fit models, and models that differ by $\pm 2\,\sigma$ in the fitting parameters. The profiles of the best fit models are remarkably similar, and we return to this point in Section 5.3. The mean signal in the BIMA dataset used to fit the models is shown on the plots (filled circle) with $\pm 2\,\sigma$ error bar. The binning introduces an uncertainty (and/or bias) in the appropriate (u, v) distance for the data point, that is not present in the model fitting procedure. For each type of model, we have adopted the (u, v) distance that provides a match with the best-fit model. This is motivated by purely graphical reasons, but we note that the mean baseline length weighted by the signal to noise of the best fit model (for constant noise on each baseline) provides an essentially indistinguishable (u, v) coordinate. However, the greater spread of the fitted models compared to the binned data point demonstrates the effect of this "smearing" of the signal in (u, v) distance.

The plots in Figure 1 also show $\pm 2\,\sigma$ confidence intervals of an azimuthally averaged synthetic visibility profile derived from the Tafalla et al. (2003) MAMBO map of L694–2. The visibility profiles are computed assuming the MAMBO map to be the true intensity

distribution convolved with a Gaussian beam of $11''$ FWHM. No assessment has been made for systematic errors in the profile due to chopping and subsequent reconstruction of the MAMBO observations. The synthetic confidence intervals are extended until the the signal to noise drops below 2 (i.e. the intervals become consistent with zero signal).

5.2.1. Systematic Uncertainties

Table 3 lists the main sources of systematic uncertainty along with the level of uncertainty they produce in the fitted density parameters (ξ_{max}, r_0, p, & H). The various systematic errors are discussed below, in rough order of importance:

Dust temperature distribution.— This is the largest source of systematic uncertainty. The temperature distribution that has been assumed in the analysis varies from ~ 8 K at the center to ~ 14 K in the outer regions, and it is motivated by physical argument. Nevertheless, the profile is probably uncertain at the level of ± 2 K. To study the effect of this uncertainty on the inferred density structure, we have repeated the analysis for each model, replacing the physical temperature distribution with an isothermal distribution at 12 K. The removal of the central minimum in the temperature profile results in a given density model producing a steeper emission profile and a shallower visibility profile. The density structure inferred is therefore less centrally concentrated than with the physical temperature profile. The effect is of a similar magnitude for all of the models: the best-fit parameters are changed by close to 2 σ.

Unresolved compact component.— The PdBI data limit the maximum contribution to the emission from an unresolved compact component: $F_c < 2.7$ mJy (3 σ). Including a dimmer compact component in the model fitting essentially reduces the visibility amplitude that is attributable to the envelope and results in fitted density structures that are more shallow. For a point source flux of $F_c = 2$ mJy, the density structure parameters are changed by roughly 1 σ.

Central position.— The flatness of the inner density profile and the lack of a detected compact component make the appropriate central position for the L694–2 core uncertain. However, the baselines of the BIMA visibilities from which the density structure is inferred are short and correspond to a fringe size of $\sim 20''$. This means that the results are not very sensitive to small changes in the adopted central position (the pointing center of the PdBI observations). The signal in the combined visibilities peaks at 10 mJy within $1''$ of the adopted central position — the peak of $N_2H^+(1–0)$ emission. A shift in the central position of $5''$, i.e. the shift between the fitted center from the extinction study and central position

assumed here, leads to a ~ 2 mJy reduction in the binned signal and a $1\,\sigma$ change in the density structure parameters, corresponding to shallower density profiles.

Extended structure.— A leading source of systematic uncertainty in the L694–2 extinction study was the effect of the contribution of the extended structure in which the core appears to be embedded (Harvey et al. 2003b). Including this additional component to the models lead to inferred core density profiles that were significantly more steep, consistent with Plummer-like and isothermal cylinder models. In the present study, this uncertainty has much smaller effect on inferred structure. Since the extended structure must be largely resolved out by the interferometers, neglecting the extended structure entirely leads to only a 10% increase in the amplitudes of the visibility profiles of the model cores. Repeating the fitting analysis for the two types of model in this context results in inferred density profiles that are $\sim 0.5\,\sigma$ more shallow.

Outer boundary.— The outer boundary of the L694–2 core has little effect in the modeling due to the limited field of view of BIMA and PdBI. For BIMA, the intensity distribution at the assumed outer edge of the core is suppressed by a factor ~ 0.05 due to the antenna pattern. Moreover, the intensity at the edge is already lower than the intensity at the center by a factor of ~ 500 (Fit I). Modifying the outer boundary therefore has no effect on the shape of the inferred density profile. However, for the Bonnor-Ebert sphere (Fit I), changing the outer radius does modify the density structure parameter ξ_{max} because this parameter describes the dimensionless profile, not the physical profile. For this fit, the alternative structure parameter, the scale radius $r_0 = R_{\mathrm{out}}/\xi_{\mathrm{max}}$ is unchanged.

Dust opacity spectral index.— The dust opacity adds systematic error via the use of the spectral index to transform the flux normalization from MAMBO to the frequency at which our observations were made. To some extent, the appropriate MAMBO frequency itself depends on the spectral index, because of the broad bandwidth used in the single dish bolometer observations. The spectral index of the dust opacity should lie in the range $\beta =$1–2. We have used $\beta = 1$ throughout; an alternative extreme, $\beta = 2$, leads to only a 4% reduction in the flux normalization, and to inferred density structure that is more shallow, but to a degree that is negligible in comparison to the other sources of error (both systematic and random).

5.3.   Discussion: A Physical Density Distribution for L694–2

The fitted physical models demonstrate clearly that the steep density gradient observed in the $r > 30''$ region with extinction (Harvey et al. 2003b) does not continue in the inner

region that could not be probed in that study. This is consistent with the modeling of single dish dust emission observations by Visser (2000) and Tafalla et al. (2003).

The visibility profiles of the best fit models shown in Figure 1 are remarkably similar to each other, only the power law model differing enough to be distinguishable by eye, and then only at long baselines. This provides an interesting demonstration of the degeneracy of the various models for starless core density structure. Figure 2 presents a plot of the best-fit density models. The normalization of the density assumes an opacity of $\kappa_{1.3\mathrm{mm}} = 0.02$ cm^2 g^{-1}, which is uncertain by a factor of ~ 5 or more (Ossenkopf & Henning 1994). At large radii the Bonnor-Ebert and Power-law models differ from the Plummer-like and cylinder models due to the fact that the latter models are assumed to be embedded in an extended uniform distribution of gas. The Plummer-like and Bonnor-Ebert models are almost identical, and have central densities that differ by only 5% ($n(\mathrm{H_2}) = 1.4 \times 10^5$ cm^{-3} with uncertainty $\sim 50\%$). The density profile of the end-on cylinder departs significantly from the the Bonnor-Ebert and Plummer-like profiles. The profile is more shallow with much lower central density ($n(\mathrm{H_2}) = 5.1 \times 10^4$ cm^{-3} with uncertainty $\sim 30\%$). This occurs despite the identical form of the expressions for the cylinder and Plummer-like models (with $R_0 = \sqrt{8}H$), and the fact that the cylinder and Bonnor-Ebert models both represent a balance between self-gravity and thermal pressure. The difference derives from the lower dimensionality of the cylindrical model; a given line-of-sight corresponds to a constant "radius", and hence there is no radial integration that for the spherically symmetric models makes the column density profiles more shallow than the density profiles. In addition, the extension of the cylinder along the line-of-sight means that the densities are correspondingly lower at a given radius. The asymmetry of the L694–2 core viewed in extinction provides a basis for preferring the cylindrical model over the others. A tilted cylinder with $H = 13.5$, $L \sin \phi = 0.14$ pc ($L \simeq 0.2$–0.5, and $\phi \simeq 20$–45°), and central density ($n(\mathrm{H_2}) = 4 \times 10^4$ cm^{-3} embedded in a uniform distribution of gas with column density $N(H + H_2) \sim 6 \times 10^{21} (L/0.5$ pc$)$ cm^{-2}, successfully reproduces the dust emission visibility profile, as well as the profile and asymmetry of the dust extinction map. The instability of the cylindrical model along its axis is also consistent with the inward motions in L694–2 inferred from molecular spectral lines (Lee, Myers & Tafalla 2001).

As already noted, the inner power law index of the fitted broken power law model ($p = 0.9\,^{+0.12}_{-0.16}$, Fit II) may be construed both as a "mean" index in the $r < 30''$ region, and as an upper limit on the index in the innermost regions (due to the trade-off between turn-over radius and power law index in the inferred visibility profile). The former is illustrated by the fact that the radially averaged "mean" effective power law index for the best-fit Plummer-like model is $\bar{p} = 0.86$ over the range in radius $0 \leq r \leq R_0$ (with $R_0 = 26''$). The profile is consistent with the Visser (2000) study who found that a similar index ($p = 0.8$) and turn-over radius ($R_0 = 32''$) reproduced the SCUBA map. The index in the inner region is

much less than that observed in the outer envelope and shows that the density distribution in the inner region of the L694–2 core has clearly not relaxed fully, along the lines assumed in the inside-out collapse of Shu (1977), despite the presence of extended inward motion in the gas (Lee et al. 2001). These inward motions may reflect the contraction of a prolate core along its major axis (Harvey et al. 2003b).

6. Summary

We present a study of the density distribution of the candidate contracting starless core L694–2 using high resolution 1.3 mm dust continuum observations from BIMA and the IRAM PdBI. In summary:

1. The PdBI visibility data span baselines from 12 to 80 kλ (spatial scales from ~ 500 to ~ 5000 AU) and do not detect any significant emission from the core. This provides a stringent constraint on the maximum point source flux: $F_c < 2.7$ mJy (3 σ). This flux limit corresponds to a very small disk mass, $M \lesssim 5 \times 10^{-4}$ M$_\odot$ (60 K/$T_{\rm disk}$), and bolsters the "starless" interpretation of the L694–2 core.

2. The BIMA visibility data in the baseline range 5 to 10 kλ (spatial scales $\sim 10^3$–10^4 AU) detect emission from the core and are used to constrain models for the density structure. That no signal is evident on baselines beyond 10 kλ confirms the flat emission profile in the inner regions, and a significant change in behavior from the steep density profile for $r \gtrsim 8000$ AU inferred from near infrared extinction of background stars (Harvey et al. 2003b). We fit four types of model for starless core density structure that can match the steep density gradient in the outer regions inferred from extinction. We adopt a temperature distribution that decreases in the inner regions due to shielding from the ISRF (Evans et al. 2001). The best fit Bonnor-Ebert sphere has dimensionless outer radius $\xi_{\rm max} = 18\,^{+3}_{-4}$ (1 σ). The best fit Plummer-like model has turn-over radius $R_0 = 26\,''\,^{+4}_{-3}\,''$ (6500^{+1000}_{-750} AU). The best fit broken power law model has index $p = 0.9\,^{+0.12}_{-0.16}$ (this model uses the maximum allowable turn-over radius of $R_0 = 30''$ (7500 AU) and provides an upper limit on the index at the center of the core). The best fit end-on isothermal cylinder has scale height $H = 12\,''\,^{+3.0}_{-1.5}\,''$ (3000^{+750}_{-400} AU).

3. We consider the effects of various sources of systematic uncertainty on the derived density structure. The largest uncertainty comes from the dust temperature distribution; assuming an isothermal core modifies the best fit parameters by $\sim 2\,\sigma$, and makes the inferred density profiles more shallow. A possible weak compact component to the emission ($F \sim 2$ mJy) and the appropriate central position ($\delta\theta \lesssim 4''$) are the main

remaining sources of uncertainty. Both of these uncertainties lead to $\sim 1\,\sigma$ changes in the inferred model parameters, again to shallower density profiles.

4. The density profiles of the various best-fit models are nearly indistinguishable at baselines shorter than ~ 10 kλ. There is a strong degeneracy between the models for starless core density structure. The two physical models (B-E sphere and isothermal cylinder) represent a balance between self-gravity and thermal pressure, and therefore they produce similar profiles. The asymmetry of the L694–2 core evident in the extinction map may provide a basis for favoring the cylindrical model. A cylinder slightly tilted to the line-of-sight with $H = 13.5''$, $L \sin\phi = 0.14$ pc ($L \simeq 0.2$–0.5, and $\phi \simeq 20$–$45°$) and central density ($n(\mathrm{H_2}) = 4 \times 10^4$ cm^{-3} embedded in a uniform distribution of gas with column density $N(H + H_2) \sim 6 \times 10^{21}$ ($L/0.5$ pc) cm^{-2} reproduces both the dust emission and extinction measurements.

REFERENCES

André, P., Ward-Thompson, D., & Barsony, M. 2000, in Protostars and Planets IV, eds. V. Mannings, A.P. Boss and S.S. Russell, (Tucson: University of Arizona Press), p. 51

Beckwith, S.V.W., Sargent, A.J., Chini, R.S. & Güsten, R. 1990, AJ, 99, 924

Benson, P.J., & Myers, P.C. 1989, ApJS, 71, 89

Black, J.H. 1994, ASP Conf. Ser. 58, The First Symposium on the Infrared Cirrus and Diffuse Interstellar Clouds, ed. R.M. Cutri & W.B. Latter (San Francisco: ASP), 355

Bonnor, W. 1956, MNRAS, 116, 351

Boss, A.P., & Hartmann, L.W. 2001, ApJ, 562, 842

Chandrasekhar, S. 1967, in An Introduction to the Study of Stellar Structure, (Dover, Toronto), p. 156

Ciolek, G.E., & Basu, S. 2000, ApJ, 529, 925

Doty, S.D., & Neufeld, D.A. 1997, ApJ, 489, 122

Draine, B.T. 1978, ApJS, 36, 595

Ebert, R. 1955, *Z.Astrophys.*, 37, 217

Evans, N.J.II, Rawlings, J.M.C, Shirley, Y.L., & Mundy, L.G. 2001, ApJ, 557, 193

Foster, P.N., & Chevalier, R.A. 1993, ApJ, 416, 303

Galli, D., Walmsley, M., & Gonçalves, J. 2002, A&A, 394, 275

Harvey, D.W.A., Wilner, D.J., Alves, J.F., Chen, H., Lada, C.J. & Myers, P.C. 2001, ApJ, 563, 903

Harvey, D.W.A, Wilner, D.J., Di Francesco, J., Lee, C.-W., Myers, P.C., & Williams, J.P. 2002, AJ, 123, 3025

Harvey, D.W.A., Wilner, D.J., Myers, P.C., Tafalla., M., & Mardones, D. 2003a, ApJ, 583, 809

Harvey, D.W.A., Wilner, D.J., Lada, C.J., Myers, P.C. & Tafalla, M. 2003b, ApJ, *submitted*

Henriksen, R., Andre, P., & Bontemps, S. 1997 å, 323, 549

Hogerheijde, M.R., van Dishoeck, E.F., Salverda, J.M. & Blake, G.A. 1999, ApJ, 513, 350

Keene, J. & Masson, C.R. 1990, ApJ, 355, 635

Lee, C.W., Myers, P.J., & Tafalla, M. 2001, ApJS, 136, 703

Lee, C.W., Myers, P.J., & Tafalla, M. 1999, ApJ, 526, 788

Mundy, L.G., Looney, L.W. & Welch W.J. 2000, in *Protostars and Planets IV*, eds. V. Mannings, A.P. Boss and S.S. Russell, (Tucson: University of Arizona Press), p. 355

Myers, P.C., & Lazarian, A. 1998, ApJ, 507, 157

Ossenkopf, V. & Henning, T. 1994, A&A, 291, 943

Ostriker, J. 1964, ApJ, 140, 1056

Plummer, H.C. 1911, MNRAS, 71, 460

Press, W.H., Teukolsky, S.A., Vetterling, W.T., & Flannery, B.P. 1992, Numerical Recipies in C, p. 691

Shirley, Y.L., Evans, N.J.II, & Rawlings, J.M.C. 2002, ApJ, 575, 337

Shirley, Y.L., Evans, N.J.II, Rawlings, J.M.C., & Gregersen, E.M. 2000, ApJS, 131, 249

Shu, F.H. 1977, ApJ, 214, 488

Shu, F. H., Adams, F.C., & Lizano, S. 1987, ARA&A, 25, 23

Tafalla, M., et al. 2003, *in preparation*

Takahashi, T., Silk, J., & Hollenbach, D.J. 1983, ApJ, 275, 145

Visser, A. 2000, Ph.D. thesis, University of Cambridge (UK)

Visser, A.E., Richer, J.S., & Chandler, C.J. 2001, MNRAS, 323, 257

Ward-Thompson, D., Motte, F., & Andre, P. 1999, MNRAS, 305, 143

Whitworth, A.P., & Ward-Thompson, D. 2001, ApJ, 547, 317

Zucconi, A., Walmsley, C.M., & Galli, D. 2001 A&A, 376, 650

Table 1.   Summary of instrumental parameters

Parameter	PdBI Value	BIMA Value
Observation dates	2001 Nov. 20;	2001 Sep. 22; Sep. 29;
	2002 Apr. 03	2002 Mar. 31 Jun. 08; Sep. 09
Configuration	D (four ants.); D (six ants.)	D; D; C; D; D (nine ants.)
Pointing center (J2000)	$19^h41^m04\rlap{.}''44$, $+10°57'00\rlap{.}''9$	$19^h41^m04\rlap{.}''32$, $+10°57'06\rlap{.}''1$
Observing frequency	231.3 GHz	231.3 GHz
Phase calibrators	J1751+096, J1925+211	J1925+211
Bandpass calibrator	3C 345; 3C 273	Uranus
Flux calibrator	MWC 349	Uranus
Primary beam FWHM	$22''$	$50''$
Bandwidth	480 MHz	700 MHz
RMS	0.9 mJy	1.6 mJy

Table 2.   Summary of the Density Model Fits

Fit	Density Model	Fitted Model Parameter	Calibration scaling	χ^2_ν
I	Bonnor-Ebert	$\xi_{\mathrm{max}} = 18\,^{+3}_{-4}$	$M = 0.90 \pm 0.04$	1.2520
II	Plummer-like	$R_0 = 26''\,^{+4}_{-3}\,''$	$M = 0.90 \pm 0.05$	1.2521
III	Broken Power Law	$p = 0.9\,^{+0.12}_{-0.16}$	$M = 0.92 \pm 0.04$	1.2519
IV	Cylinder	$H = 12''\,^{+3.0}_{-1.5}\,''$	$M = 0.90 \pm 0.05$	1.2520

Table 3.   Summary of systematic uncertainties in fitted parameters

Model Assumption	Variation	Resulting Systematic Error (σ) [1]
Temperature distribution	$T_d = T_{\mathrm{phys}}(r) \longrightarrow 12$ K	~ 2
Central point source flux	$F \sim 2$ mJy	~ 1
Central position	$\delta\theta \lesssim 4''$	~ 1
Neglect extended structure [2]	$F_0(r < 30'') = 80$ mJy $\longrightarrow 0$	~ 0.5
Outer boundary of L694–2 [3]	$\delta R_{\mathrm{out}}/R_{\mathrm{out}} \lesssim 50\%$	$\ll 1$
Dust opacity spectral index	$\beta = 1 \longrightarrow 2$	$\ll 1$

[1]Systematic error in the fitted model parameter given in units of σ the random error in the parameter listed in Table 2. Note that each quoted systematic error corresponds to a *shallowing* of the inferred density profile.

[2]Applies to Plummer-like and Cylinder models only

[3]Does not apply to B-E sphere; for the B-E model, increasing the outer radius increases ξ_{max} in proportion to R_{out}, keeping constant scale radius r_0
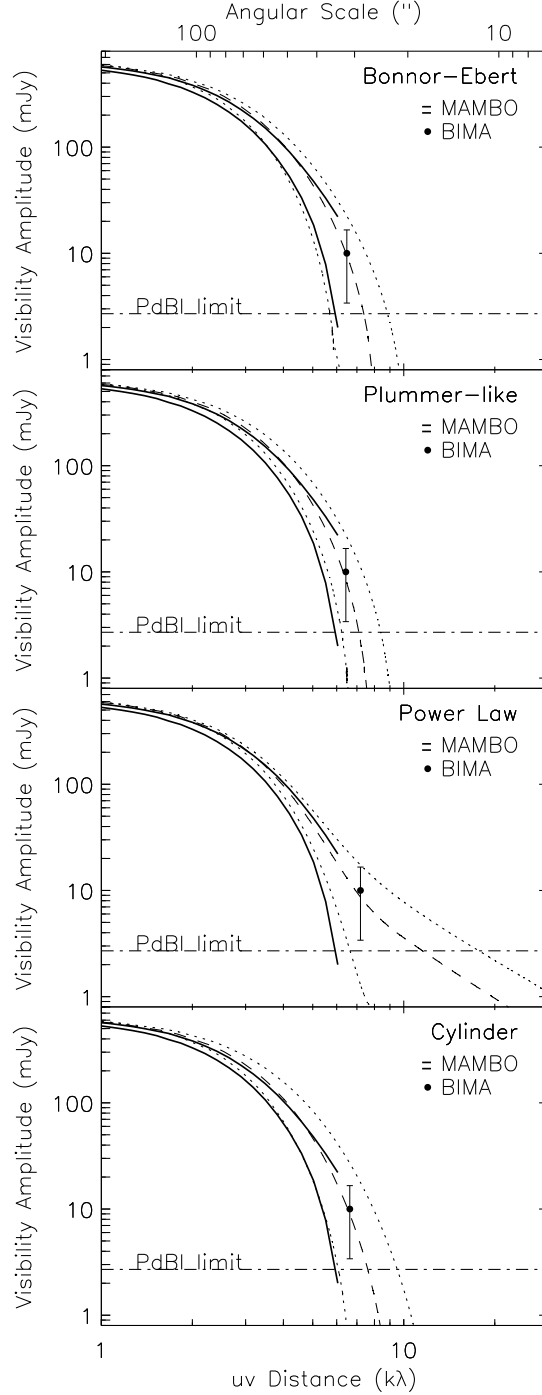
Fig. 1.— Visibility amplitude vs. (u, v) distance for L694–2 at 1.3 mm, for the best-fitting models (dashed lines) and models that deviate by $\pm 2\,\sigma$ in the fitting parameters (dotted lines). The binned BIMA visibility amplitude in the baseline range 5 to 10 kλ is also shown (circle), with a $\pm 2\,\sigma$ error bar. The PdBI limit on a point-like component (> 12 kλ) is shown as a horizontal (dash-dot) line. The solid lines represent $\pm 2\,\sigma$ intervals of the azimuthally averaged synthetic visibility profile derived from the MAMBO map. See text for further explanation.
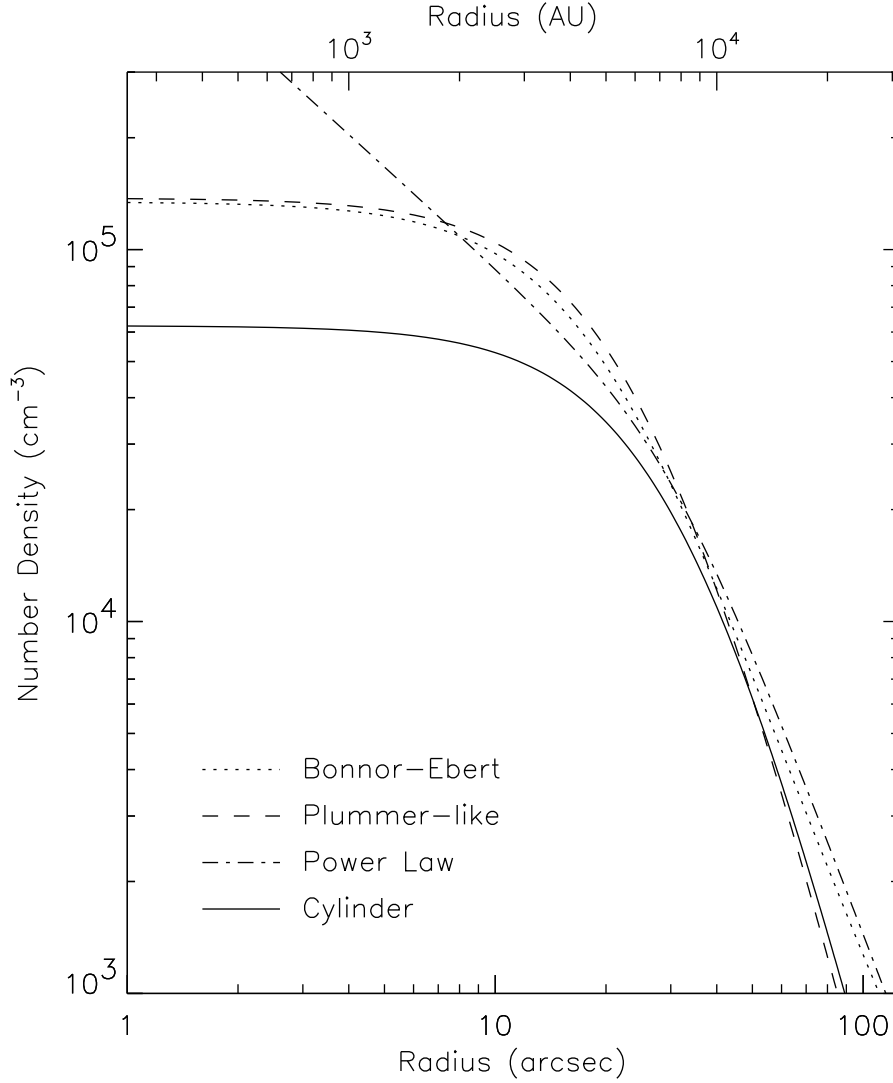
Fig. 2.— Number density of molecular hydrogen vs. radius for the various best fit models of L694–2. The number density calculation assumes a dust opacity of $\kappa_{1.3\text{mm}} = 0.02$ cm^2 g^{-1}, a mean molecular weight of $\mu = 2.29$, and a Hydrogen mass fraction $X_{\text{H}} = 0.73$. The best-fit Bonnor-Ebert (*dotted*) and Plummer-like (*dashed*) profiles are nearly identical. The cylindrical model (*solid*) has density a factor ~ 2 lower due to the extension of the cylinder along the line-of-sight.